ACS PHYSICAL CHEMISTRY Au
AN OPEN ACCESS JOURNAL OF THE AMERICAN CHEMICAL SOCIETY

pubs.acs.org/physchemau
Article

Unveiling the Photoactivation Mechanism of BLUF Photoreceptor Protein through Hybrid Quantum Mechanics/Molecular Mechanics Free-Energy Calculation

Masahiko Taguchi, Shun Sakuraba, Justin Chan, and Hidetoshi Kono*

Cite This: ACS Phys. Chem Au 2024, 4, 647−659
Read Online
ACCESS | Metrics & More | Article Recommendations | Supporting Information

ABSTRACT: OaPAC is a photoactivated enzyme that forms a homodimer. The two blue-light using flavin (BLUF) photoreceptor domains are connected to the catalytic domains with long coiled-coil C-terminal helices. Upon photoreception, reorganization of the hydrogen bonding network between Tyr6, Gln48, and the chromophore in the BLUF domain and keto−enol tautomerization of Gln48 are thought to occur. However, the quantitative energetics of the photoisomerization reaction and how the BLUF domain's structural change propagates toward the catalytic domain are still unknown. We evaluate the free-energy differences among the dark-state and two different light-state structures by the free-energy perturbation calculations combined with QM/MM free-energy optimizations. Furthermore, we performed long-time MD simulations for the free-energetically optimized dark- and light-state structures to clarify the differences in protein dynamics upon photoisomerization. The free-energy difference between the two optimized light-state structures was estimated at ∼4.7 kcal/mol. The free-energetically optimized light-state structure indicates that the chemically unstable enol tautomer of Gln48 in the light state is stabilized by forming a strong hydrogen bonding network with the chromophore and Tyr6. In addition, the components of free-energy difference between the dark- and light-state structures show that the energy upon photoreception is stored in the environment rather than the internal photoreceived region, suggesting a mechanism to keep the photoactivated signaling state with the chemically unstable enol tautomer of Gln48. In the light state, a fluctuation of Trp90 near the C-terminal helix becomes large, which causes subsequent structural changes in the BLUF core and the C-terminal helix. We also identified residue pairs with significant differences concerning residue-wise contact maps between the dark and light states.

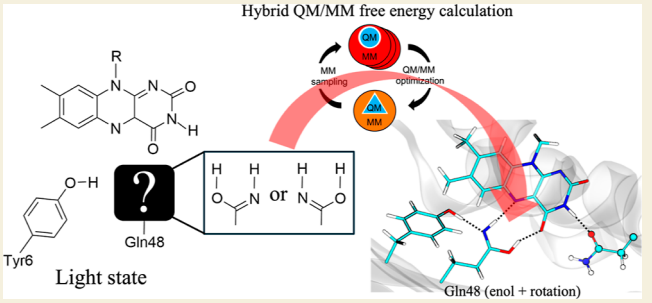

KEYWORDS: *BLUF protein, photoactivation, molecular simulation, hybrid quantum mechanics/molecular mechanics method, free energy calculation*

INTRODUCTION

Cyclic adenosine monophosphate (cAMP) is one of the second messengers for intracellular signal transduction. It is involved in cellular processes such as the elongation and differentiation of axons in neurons.[1] Membrane-integral adenylate cyclase synthesizes cAMP from adenosine triphosphate via its activation by GTP-binding protein,[2] whereas photoactivated adenylate cyclase (PAC) directly synthesizes cAMP by light activation.[3] This unique photoswitch function of PAC is currently utilized as a new optogenetics tool to control the intracellular cAMP concentration noninvasively and precisely in time and space instead of pharmacological methods.[1,4−8] The optogenetics technique with PAC helps elucidate axonal morphogenesis[1] and may have a medical application for understanding the mechanisms of diseases relating to it.[7]

PACs have different catalytic reaction abilities and rising catalytic activity times after photoactivation.[9−11] For example, PAC from *Beggiatoa* (bPAC) has ∼100 times higher catalytic activity in the light than in the dark state.[9] Also, PAC from *Oscillatoria acuminata* (OaPAC) has the lowest catalytic activity in the dark state among PACs, enabling fine control of cAMP production.[10] Mutant PACs with no dark activity rapidly increasing cAMP more than 1000 times upon light irradiation were developed.[11]

Recently, molecular structures of PAC were solved by X-ray crystallography at the atomic level, and the characteristic molecular shape was revealed.[10,12,13] PAC is a homodimer protein, and each protomer consists of two domains: the photoreceptor domain called sensors of blue-light using flavin

Received: May 19, 2024
Revised: August 18, 2024
Accepted: October 7, 2024
Published: October 29, 2024

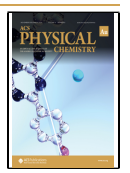

https://doi.org/10.1021/acsphyschemau.4c00040
ACS Phys. Chem Au 2024, 4, 647−659

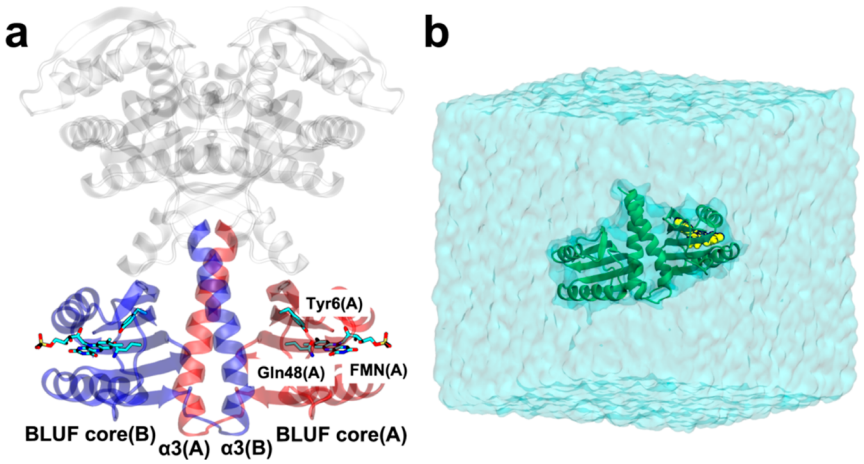

Figure 1. Structure of the BLUF-dimer and its molecular simulation system. (a) Crystallographic structure of OaPAC in the dark state (PDB ID: *4YUS*). The protein backbone is drawn in ribbon representation. The monomers A and B are colored in red and blue, respectively. Heavy atoms of the chromophore and the side chains of Tyr6 and Gln48 are depicted in stick representation. Carbon, oxygen, nitrogen, sulfur, and phosphorus atoms are colored in cyan, red, blue, yellow, and gold, respectively. (b) QM/MM simulation system for the dark state in a periodic boundary condition. Quantum mechanically treated molecules are depicted in van der Waals representation colored in yellow.

(BLUF) and the catalytic domain called AC (Figure 1a). The BLUF domain includes the conserved core region (residues 1−102 in Figure S1) and the chromophore flavin mononucleotide (FMN), whose maximum absorption wavelength is ∼450 nm, and also the long C-terminal helix (residues 103−126 in Figure S1) called α3, which connects the BLUF domain to the AC domain (Figure 1a). The two α3 helices from each protomer form a coiled-coil structure (Figure 1a). This structure is in contrast to that of BlrP1, whose BLUF domains are separated from each other.[14] In PAC, the activation region of the BLUF domain is 45 Å from that of the AC domain. The molecular mechanism of how light-absorption information in the BLUF domain transmits to the AC domain and regulates the catalytic reaction is still unknown.

The BLUF domain was found through studies of photoavoidance in *Euglena gracilis*[3] and photosynthesis gene expression in *Rhodobacter sphaeroides*.[15] It is experimentally known that the maximum absorption wavelength of the BLUF domain red shifts ∼10 nm upon blue-light reception.[10,15] However, the details of the photochemical reaction have not yet been clarified. Moreover, since the structural difference of X-ray crystallographic structures of OaPAC between the dark state (PDB ID: 4YUS)[10] and the light state (PDB ID: 5X4U)[12] is very small (C_α-RMSD ∼ 0.3 Å), how the structural change of the photoreceptor domain controls the catalytic activity of the catalytic domain is not revealed yet.

In most photoreceptor proteins such as rhodopsin, phytochrome, photoactive yellow protein, and LOV protein, chromophore undergoes characteristic structural change upon photoreception, inducing large conformational change.[16] On the other hand, in the BLUF domain, it was known that the chromophore itself does not undergo characteristic structural change upon photoreception by ultraviolet−visible absorption spectroscopy,[15] and only the hydrogen bonding network with amino acid residues near the chromophore changes.[17] Up to now, the photochemical reaction and the subsequent protein structural change have been extensively studied structurally,[18−24] spectroscopically,[25−42] and computationally.[43−62]

In the BLUF domain, well-conserved Tyr6 and Gln48 near the chromophore FMN are shown to be essential for photoactivation by the mutational experiments.[18,24,25,29,31,32,40,42] Infrared spectroscopy experiments showed that the ∼10 nm red shift of the absorption wavelength corresponds to the downshift of the C4═O vibration of FMN.[26−28] This indicates that the hydrogen bonds between FMN and Gln48 become stronger in the light state. To date, by a combination of the orientation and amide-iminol tautomerization of the Gln48 side chain (hereafter, we call this keto−enol tautomerization following refs 32−35, 38, 42, 46, 55, 59, and 62), various scenarios for chemical and structural changes of Gln48 from the dark state to the light state were proposed.[29−33,37,38,41,43,44]

Using Fourier transform infrared (FTIR) spectroscopy, isotope exchange method, and quantum mechanical/molecular mechanical (QM/MM) calculation, Domracheva et al. identified the dark-state structure of Tyr6-Gln48-FMN. They proposed that the Gln48 side chain undergoes rotation and keto−enol tautomerization in the light state.[37] Later, using FTIR spectroscopy and QM/MM calculation, Iwata et al. comprehensively investigated the possible hydrogen bonding patterns of Tyr6-Gln48-FMN from the dark state to the light state.[38] They concluded that the Gln48 side chain undergoes a rotation and keto−enol tautomerization in the light state. A recent study by Hontani et al. using Raman spectroscopy and QM calculation also supports the simultaneous rotation and tautomerization.[41] On the other hand, the X-ray crystallographic structures of PAC solved for both dark and light states do not show the rotation of the Gln48 side chain.[10,12,13] As Iwata et al. discussed,[38] distinguishing the oxygen and nitrogen atoms in X-ray crystallographic experiments is technically challenging; there remained the possibility that two atoms were assigned opposite elements.

In this study, we computationally investigate two light state models: the one proposed from spectroscopic experiments[38,41] and the other obtained from X-ray crystallographic structures;[12,13] in other words, the enolized state with or without rotation of the Gln48 side chain. To model the simulation systems accurately, we compare both models quantitatively, based on the calculation of the free energy difference. Then, we clarify the structural difference between the dark- and light-state models of the BLUF domain and discuss the photoactivation mechanism.

https://doi.org/10.1021/acsphyschemau.4c00040
ACS Phys. Chem Au 2024, 4, 647−659

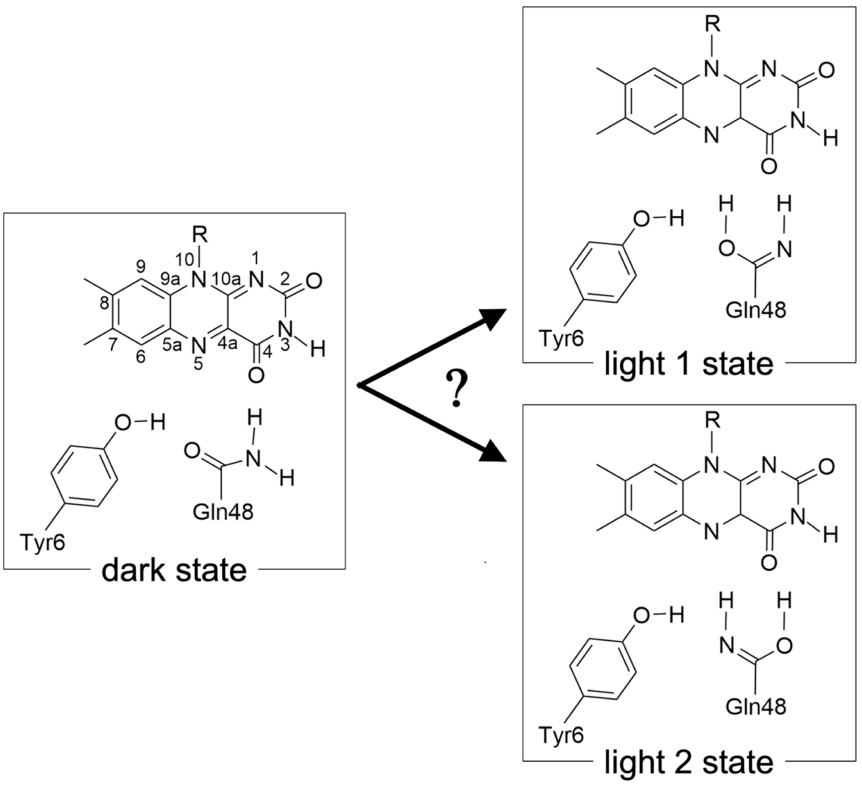

Figure 2. Proposed scheme of the photoisomerization reaction of the chromophore, Tyr6, and Gln48 upon blue-light absorption. The side chain of Gln48 takes the usual keto form in the dark state; it changes to the enolized form in the light state without/with rotation of the side chain (light 1/2 state).

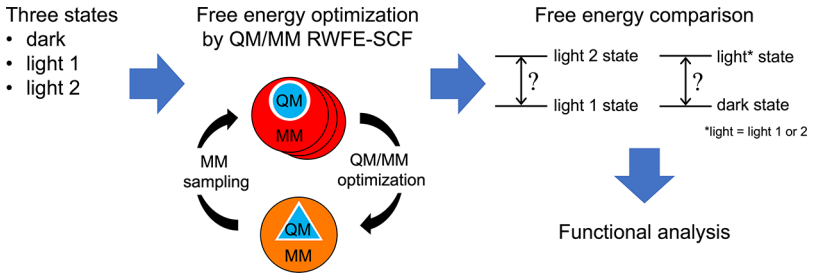

Figure 3. Summary of this study. Simulation models of the dark, light 1, and light 2 states of the BLUF-dimer were prepared (note that only the monomer A is treated as QM/MM; see Methods). First, the three state structures were free-energetically optimized by the QM/MM RWFE-SCF method. Then, the free-energy differences among the optimized three state structures were evaluated. Finally, the functional analysis of long-time MD simulation trajectories of the dark and light states was performed.

Since the enolized state is chemically unstable in general and its electronic state is complex, describing the enolized state in the classical molecular dynamics simulation with the molecular force field is difficult. In this study, we employ a hybrid QM/MM free-energy method called the QM/MM RWFE-SCF method, which enables a compatible description of a highly accurate ab initio calculation for a reaction center, including the chromophore and its interaction with statistically ample conformational sampling of the MM protein environment as well as solvent by long-time atomic-level molecular dynamics simulations.[63,64] For the BLUF dimer with long C-terminal coiled-coil helices characteristic of PAC, we evaluated the free-energy difference between two modeled light states using free-energy perturbation (FEP) calculations[65] and analyzed the structural response of the protein upon photoactivation. We verified the modeled structures by evaluating the absorption wavelength based on the excited-state calculations. Through analysis of different contact maps between the dark and light states, we found that residues that have the most significant contact difference between the dark and light states are Trp90 and Met92, crucial for photoactivation shown by mutational experiments.[23,24,32,36,39,40,66−68] We also assessed the subsequent residues with the significant contact difference.

METHODS

Overview of the Method

First, simulation models of dark, light 1, and light 2 states were prepared (Figures 1 and 2). Then, the three state structures were free-energetically optimized by the QM/MM RWFE-SCF method.[63,64] Next, the free-energy difference among the optimized three-state structures was evaluated by FEP.[65] Finally, functional analysis of long-time MD simulation trajectories in the dark and light states was performed. The schematic overview of this study is summarized in Figure 3.

https://doi.org/10.1021/acsphyschemau.4c00040
ACS Phys. Chem Au 2024, 4, 647−659

System Preparation

The initial structure was constructed with a crystallographic protein structure of the BLUF domain dimer of OaPAC in the dark state (PDB ID: 4YUS)[10] (Figures 1a and S1). Missing hydrogen atoms were added to the protein and FMN with the LEaP module of AMBER18.[69] Standard protonation states for the titratable groups of the protein were set. Protonation of histidine residues (His70 and His119) was put on the epsilon and delta nitrogen atoms, respectively, by examining the surrounding environment. The phosphoric acid of FMN was assumed to be deprotonated. The C-terminal residue (Thr126) was capped with NME. The protein with FMN was immersed in a periodic boundary box (100.9 × 100.7 × 101.0 Å^3) filled with TIP3P water molecules[70] (Figure 1b), and 88 Na^+ ions and 76 Cl^- ions were added to neutralize the systems and mimic the intracellular environment (∼150 mM NaCl). The number of atoms in the box was 88,085 in total. The force field parameter set of AMBER ff14SB[71] and that reported in ref 72 were employed for the force fields of the protein and Na^+ and Cl^- ions, respectively. Effective atomic charges of FMN for force field calculations were quantum chemically determined by the restrained electrostatic potential fitting method for the electron densities obtained by DFT calculations with the B3LYP-D3 functional[73,74] and the 6-31G** basis set (for around the phosphoric acid, the 6-31+G** basis set was used) in a polarized continuum medium water solvent model[75] after geometry optimization. The quantum chemical calculations were performed with the GAMESS2014 program package.[76] Other force field parameters of FMN were taken from GAFF2.

MD Simulation

GPU modules of the AMBER18 program package[69,77] were employed. Before the MD simulation was started, the coordinates of added hydrogen atoms, missing in the crystal structure, were energetically minimized under harmonic restraints to heavy atoms of the protein and FMN with a force constant of 3.0 kcal/(mol·Å^2). The structure was further energetically minimized under harmonic restraints to the C_α atoms of the protein and heavy atoms of FMN with a force constant of 3.0 kcal/(mol·Å^2). Next, the system was heated from 0 to 300 K for 300 ps in NVT conditions under harmonic restraints of C_α atoms of the protein and heavy atoms of FMN with a force constant of 3.0 kcal/(mol·Å^2). After the heating, the system was gradually relaxed in NPT conditions with decreasing harmonic restraints to C_α atoms of the protein and heavy atoms of FMN with a force constant of 3.0, 1.0, 0.5, 0.2, and 0.1 kcal/(mol·Å^2) for every 1 ns. Then, an MD simulation at 300 K for 1 μs in NPT conditions was performed to make the system equilibrated. In the MD simulation, lengths of bonds, including hydrogen atoms, were constrained by the SHAKE/RATTLE method.[78,79] The time step for integration was set to 2 fs. Long-range electrostatic interactions were calculated using the particle mesh Ewald method.[80] Short-range nonbonded interactions were cut off at 10 Å. Temperature and pressure were controlled with Langevin bath (collision frequency is 2 ps^{-1}) and Berendsen's methods.[81]

QM/MM RWFE-SCF Geometry Optimization

To obtain free-energetically optimized structures of the dark-state and two light-state structures, we performed QM/MM RWFE-SCF geometry optimizations. The computational scheme of the QM/MM RWFE-SCF geometry optimization includes iteration of a cycle of two calculations called sequential sampling, i.e., an MD simulation of the MM region for conformational sampling of the MM region to construct a free-energy surface of the QM region and a QM/MM geometry optimization on the free-energy surface, until simultaneous convergences of the MM statistical sampling and the QM/MM geometry optimization.[63,64] An MD simulation for the MM region under NVT conditions for 10 ns was carried out in each iteration cycle. The free-energy surface was constructed with the 50,000 conformational samples obtained from the last 5 ns of the MD trajectory. A QM/MM geometry optimization for the QM region on the free-energy surface, updating the geometry and the effective atomic charges of the QM region, was then performed.

The QM region consists of 53 atoms of the isoalloxazine ring of FMN and the side chains of Tyr6 and Gln48 in BLUF monomer A (Figure S2a). The bonding QM-MM boundaries were capped with hydrogen atoms. The DFT B3LYP-D3 functional[73,74] was used. The 6-31G** basis functions were employed, except for the boundary atoms, hydrogen atoms bonding to the boundary atoms, and cap hydrogen atoms, for which the 6-31G basis functions were used. Restraint parameters of the restrained electrostatic potential charge operators[82] were set to 0.04, except for those for the boundary atoms and the hydrogen atoms bonding to the boundary atoms, which were set to 0.4. The gradient criterion of 5.0×10^{-4} hartree/bohr was used as a criterion of the convergence of the QM/MM geometry optimization. The QM/MM RWFE-SCF calculations were performed with GAMESS2014[76] and the QM/MM interface.[63,64]

To obtain the initial geometry and effective atomic charges of the QM region for the QM/MM RWFE-SCF geometry optimization for the dark state, a cooling MD simulation from the end of the equilibrium-MD simulation at 300 to 0 K for 300 ps in *NVT* conditions was first carried out. QM/MM potential energy geometry optimizations were performed with fixed MM coordinates. The MM region was then heated to 300 K for 300 ps in *NVT* conditions with the coordinates and the effective atomic charges of the QM region fixed at the optimized one, and the iteration cycle of the QM/MM RWFE-SCF free-energy geometry optimization consisting of the MD sampling and the QM/MM geometry optimization was initiated.

The QM/MM RWFE-SCF geometry optimizations for the two light-state structures were also initiated using the abovementioned procedure. The system at 0 K was obtained by cooling simulation from the last snapshot of the QM/MM RWFE-SCF geometry optimization for the dark state. The initial geometry and charges of the QM region in the two light states, which undergo the formation of the enol form of the Gln48 residue accompanied by a proton transfer (Figures 2 and S2b), were then each obtained by QM/MM potential energy geometry optimizations with the van der Waals and intramolecular parameters of the QM/MM boundary determined by the AMBER ff14SB parameter set[71] and GAFF2 for the atoms related to the keto−enol tautomerization. Then, the QM/MM RWFE-SCF free-energy geometry optimizations were started for each. Note that we used only a dark-state crystal structure (PDB ID: 4YUS)[10] throughout this study to avoid the initial structure dependence.

Evaluation of Free-Energy Differences between the Dark State and Two Light States

To energetically characterize the dark state and two light states, free-energy differences between those states were evaluated by FEP calculations as described previously.[65] The free-energy differences between two states, X and Y, are given as

$$\Delta_{Y-X}F_{\mathrm{QM/MM}} = \Delta_{Y-X}E_{\mathrm{QM}} + \Delta_{Y-X}F_{\mathrm{QM-MM,MM}} \quad (1)$$

where the former is the difference between the expectation values of the QM Hamiltonian and the latter is the free-energy difference originating from QM−MM interactions and MM interactions in the MM region. The latter was evaluated using the FEP method with a Bennett acceptance ratio (BAR).[83−85] The former consists of two terms, which is

$$\Delta_{Y-X}F_{\mathrm{QM}} = \Delta_{Y-X}E_{\mathrm{QM,opt}} + \Delta_{Y-X}F_{\mathrm{QM,hess}} \quad (2)$$

where the first term was directly obtained by the QM/MM RWFE-SCF free-energy optimization, while the second term represents the vibrational contribution from the QM region, which can be evaluated by Hessian matrices of the free-energy surfaces obtained by QM/MM RWFE-SCF calculations.[63,64] $\Delta_{Y-X}E_{\mathrm{QM,hess}} = \Delta_{Y-X}E_{\mathrm{zero}} + \Delta_{Y-X}E_{\mathrm{vib}}$ where the first and second terms represent zero point energy and energy from vibrational entropy, respectively. For the calculation of the Hessian matrices, we used a common vibrational scaling factor for the DFT calculation at the B3LYP/6-31G** level of theory, 0.961.[86]

For the calculation of FEP, the geometry and the effective atomic charges of the QM region were changed with linearly divided, discrete points as

https://doi.org/10.1021/acsphyschemau.4c00040
ACS Phys. Chem Au 2024, 4, 647−659

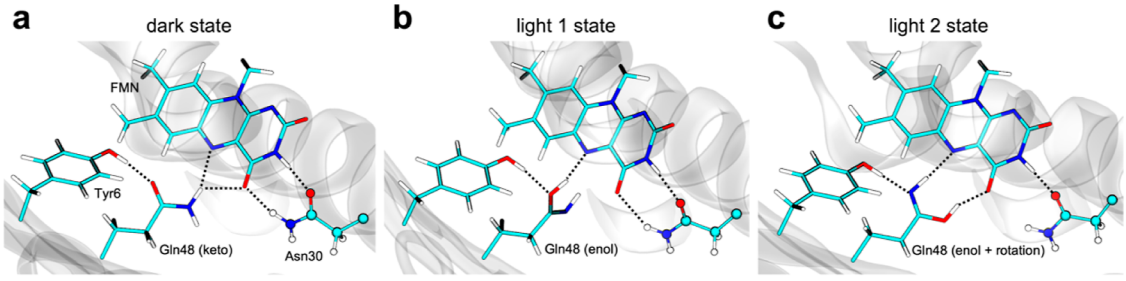

donor	acceptor	distance
Tyr6:OH	Gln48:OE1	2.65
Gln48:NE2	FMN:N5	3.10
Gln48:NE2	FMN:O4	3.17
Asn30:ND2	FMN:O4	2.91
FMN:N3	Asn30:OD1	2.83

donor	acceptor	distance
Tyr6:OH	Gln48:OE1	2.80
Gln48:OE1	FMN:N5	2.88
Asn30:ND2	FMN:O4	3.18
FMN:N3	Asn30:OD1	2.82

donor	acceptor	distance
Tyr6:OH	Gln48:NE2	2.70
Gln48:NE2	FMN:N5	3.13
Gln48:OE1	FMN:O4	2.71
FMN:N3	Asn30:OD1	2.73

Figure 4. Hydrogen bonding interactions around the FMN. (a) Dark state. (b) Light 1 state. (c) Light 2 state. The free-energy optimized structures (top) and hydrogen bond list (bottom) are shown (unit: Å). A hydrogen bond is defined as satisfying both conditions: a donor−acceptor distance within 3.2 Å and a donor−hydrogen−acceptor angle between 135° and 180°. The isoalloxazine ring of FMN and the side chains of Tyr6 and Gln48 are depicted in stick representation, and the side chain of Asn30 is depicted in ball and stick representation.

$$R(i) = \lambda_i R_Y + (1 - \lambda_i) R_X$$
$$q(i) = \lambda_i q_Y + (1 - \lambda_i) q_X$$
$$\lambda_i = \frac{i}{N-1},\ i = 0, 1 \ldots, N-1 \quad (3)$$

where $R_{X/Y}$ and $q_{X/Y}$ are the coordinates and the effective atomic charges of the QM region in the X/Y state. The Lennard-Jones and intramolecular interactions at the QM−MM boundaries were evaluated with the MM force fields.[63,65] The geometry and the effective atomic charges of the QM region were changed with linearly divided, discrete 20 points (40 points for FEP calculation between the dark and light 1 states). The MD simulation at each point was started from the last snapshot of the MD trajectory calculation at the previous point. Conformational samples of the MM region at each point were obtained by an MD trajectory calculation for 50 ns, and 50,000 samples taken from the trajectory of the last 25 ns were employed to evaluate the free-energy difference between the neighboring two points. Both forward and backward calculations were performed to assess the statistical convergence. The total length of the MD trajectory calculation was 1 μs each (2 μs each for FEP calculation between the dark and light 1 states).

Long-Time MD Simulations after the Free-Energy Geometry Optimizations and Analysis

We performed long MD simulations after the free-energy geometry optimizations to observe slower protein conformational changes, which were not observed in the free-energy geometry optimizations. Five free MD simulations were carried out for 5 μs each, with the geometries and effective atomic charges of the QM region fixed at the optimized ones for the dark and free-energetically chosen light state. These five MD simulations for the dark and light states were performed from the same free-energetically optimized structure only with changing velocity, i.e., different random numbers. The total sampling MD trajectories of the dark and light states are 25 μs each and used for structural analysis shown in the Results section. Residue-wise contact-map analysis was performed by MDTraj.[87] We defined contacts if any heavy atoms of the residue pair are within 4.5 Å. The error in residue-wise contact-map was calculated using five independent MD runs. Residue-wise root-mean-square fluctuation (RMSF) analysis, secondary structure calculations, and calculations of angles between two helices were performed by CPPTRAJ.[88]

Calculation of the Absorption Wavelength

The absorption wavelength was evaluated by using the calculation of vertical excitation energies. The vertical excitation energies were calculated with second-order extended multiconfigurational quasi-degenerated perturbation theory[89,90] (XMCQDPT2) at the free-energetically optimized structures with the MM mean field electrostatic potentials generated from long-time MD simulation for 5 μs. We employed the same QM system and basis functions as those used for free-energy geometry optimization. The XMCQDPT2 method can explicitly deal with multiconfigurational and dynamic electron correlation. Complete active space (CAS) for XMCQDPT2 calculations consists of 10 electrons in 10 valence π orbitals of FMN. Three-state-averaged CASSCF wave functions were refined by XMCQDPT2 calculations.

RESULTS

Free-Energy Optimized Structures of the Dark State and Two Light States

The free-energy optimization of the dark, light 1, and light 2 state structures required 100, 144, and 118 cycles of the sequential sampling (MD simulations for 1.00, 1.44, and 1.18 μs in total) until convergence, respectively. Our vibrational calculations showed no imaginary frequencies for the optimized structures of the dark, light 1, and light 2 states, indicating that the optimized structures were in a stable stationary state. The free-energy-optimized structures show different hydrogen interaction patterns (Figure 4). Although the hydrogen interaction between the OH atom of Tyr6 and the OE1/NE2 atom of Gln48 was kept in the three states, there are some differences (~0.1 Å) among these states. Conversely, the hydrogen between Gln48 and FMN was significantly changed. In the dark state, two hydrogen interactions exist between the NE2 atom of Gln48 and the N5 and −O4 atoms of FMN (Figure 4a). In the light 1 state, however, the hydrogen bond between the NE2 atom of Gln48 and the N5 atom of FMN vanished, and only one relatively strong hydrogen bond between the OE1 atom of Gln48 and the N5 atom of FMN (2.88 Å) was formed upon keto−enol tautomerization of Gln48 (Figure 4b). In the light 2 state, upon keto−enol tautomerization and rotation of the side chain of Gln48, there are two hydrogen interactions between the NE2/OE1 atom of Gln48 and the N5/O4 atom of FMN; the former is relatively weak (3.13 Å), while the latter is significantly strong (2.71 Å) (Figure 4c). Asn30 has two hydrogen bonds with FMN in the dark and light 1 states; however, there is only one hydrogen bond in the light 2 state (Figure 4b,c). The remarkably strong hydrogen bond between the OE1 atom of Gln48 and the O4 atom of FMN is thought

https://doi.org/10.1021/acsphyschemau.4c00040
ACS Phys. Chem Au 2024, 4, 647−659

to be consistent with the vanishment of the hydrogen bond between the ND2 atom of Asn30 and the N3 atom of FMN.

Free-Energy Differences between the Dark State and Two Light States

Free-energy differences between the light 1 and light 2 states (L1 and L2), optimized by the QM/MM RWFE-SCF methods described above, were evaluated by MD simulations of FEP calculations with the BAR method (see Methods). The free-energy difference was computed as 4.7 kcal/mol (Figure 5 and Table 1), indicating that the light 2 state is energetically more stable than the light 1 state. FEP calculation of 1 μs in the forward and backward directions provided sufficient statistical convergence for both directions, represented by a slight difference of 0.2 kcal/mol between the two directions (Table 1).

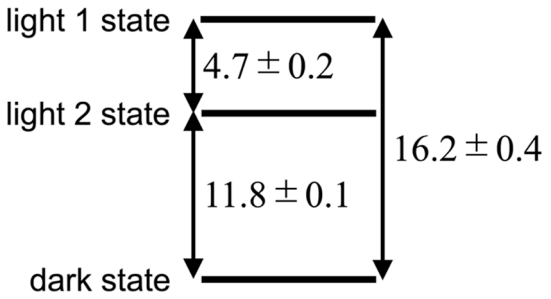

Figure 5. Summary of the free-energy differences among the dark, light 1, and light 2 states.

The free-energy difference originates from two contributions of the QM energy, the QM−MM interaction energy and the MM energy, as shown in eq 1. $\Delta_{L1-L2}E_{QM}$ gave a significant, positive contribution of 8.6 kcal/mol, indicating that the QM energy in the light 2 state was considerably lower than that in the light 1 state (Table 1). The large energy differences are mainly due to the interaction between the ring of FMN and the side chain of Gln48 because the internal energy of FMN and the interaction between Tyr6 and Gln48 are nearly equal between the light 1 and 2 states.

The isoalloxazine ring of FMN, therefore, energetically favors interaction with the rotated and enolized form of Gln48 in the light 2 state over the enolized form of Gln48 in the light 1 state. In contrast, the other contribution of $\Delta_{L1-L2}F_{QM-MM,MM}$ of −3.9 kcal/mol was negative and under-compensated $\Delta_{L1-L2}E_{QM}$ of 8.6 kcal/mol, resulting in a positive $\Delta_{L1-L2}F_{QM/MM}$ of 4.7 kcal/mol (Table 1).

The free-energy difference between the dark and light 2 states was also evaluated. The free-energy difference was assessed as 11.8 kcal/mol (Figure 5 and Table 1). Interestingly, $\Delta_{L2-D}F_{QM-MM,MM}$ of 8.3 kcal/mol is more than two times as large as $\Delta_{L2-D}E_{QM}$ of 3.5 kcal/mol, suggesting that energy upon blue light absorption is stored in the environment rather than inside the photoreceived region. The difference in QM energy between the enol and keto forms of the glutamine in the gas phase was evaluated as 14.3 kcal/mol (Table S1). The energy stored in the environment of the BLUF domain may realize the photoactivated signaling state with a chemically unstable enolized form of Gln48 that lasts for milliseconds to seconds.

The free-energy difference between the dark and light 1 states was also evaluated to check consistency. The difference was 16.2 kcal/mol (Figure 5 and Table 1). The discrepancy was within the sum of each error satisfying the thermodynamic consistency of free energy; i.e., free energy does not depend on any path between two states (Figure 5). From now on, we treat the light 2 state as the light state.

Structural Analysis of the Dark and Light States

We used the trajectory of long-time MD simulation for the dark and light states after the free-energy optimizations (see Methods).

In the dark state, Met92 forms a weak hydrogen bond with Gln48.[12] In the light state, Gln48 of the enol form makes

Table 1. Free Energy Differences of the Dark State and Two Light States[a]

			L1−L2			
$\Delta_{L1-L2}E_{QM,opt}$	$\Delta_{L1-L2}E_{QM,hess}$		$\Delta_{L1-L2}E_{QM}$		$\Delta_{L1-L2}F_{QM-MM,MM}$	$\Delta_{L1-L2}F_{QM/MM}$
	$\Delta_{L1-L2}E_{zero}$	$\Delta_{L1-L2}E_{vib}$				
10.2	0.2	−1.8	8.6	forward[b]	−3.7	4.9
				backward[c]	−4.1	4.5
				average[d]	−3.9	4.7
			L1−D			
$\Delta_{L1-D}E_{QM,opt}$	$\Delta_{L1-D}E_{QM,hess}$		$\Delta_{L1-D}E_{QM}$		$\Delta_{L1-D}F_{QM-MM,MM}$	$\Delta_{L1-D}F_{QM/MM}$
	$\Delta_{L1-D}E_{zero}$	$\Delta_{L1-D}E_{vib}$				
13.9	−1.2	−0.7	12.0	forward[b]	4.6	16.6
				backward[c]	3.8	15.8
				average[d]	4.2	16.2
			L2−D			
$\Delta_{L2-D}E_{QM,opt}$	$\Delta_{L2-D}E_{QM,hess}$		$\Delta_{L2-D}E_{QM}$		$\Delta_{L2-D}F_{QM-MM,MM}$	$\Delta_{L2-D}F_{QM/MM}$
	$\Delta_{L2-D}E_{zero}$	$\Delta_{L2-D}E_{vib}$				
3.7	−1.4	1.2	3.5	forward[b]	8.4	11.9
				backward[c]	8.2	11.7
				average[d]	8.3	11.8

[a] Δ_{L1-L2}FQM/MM, Δ_{L1-D}FQM/MM, Δ_{L2-D}FQM/MM, and their energy components, in kcal/mol (D, L1, and L2 represent the dark, light 1, and light 2 states, respectively). [b] Energy differences by forward sampling. [c] Energy differences by backward sampling. [d] Averages of energy differences were calculated by forward and backward samplings.

https://doi.org/10.1021/acsphyschemau.4c00040
ACS Phys. Chem Au 2024, 4, 647−659

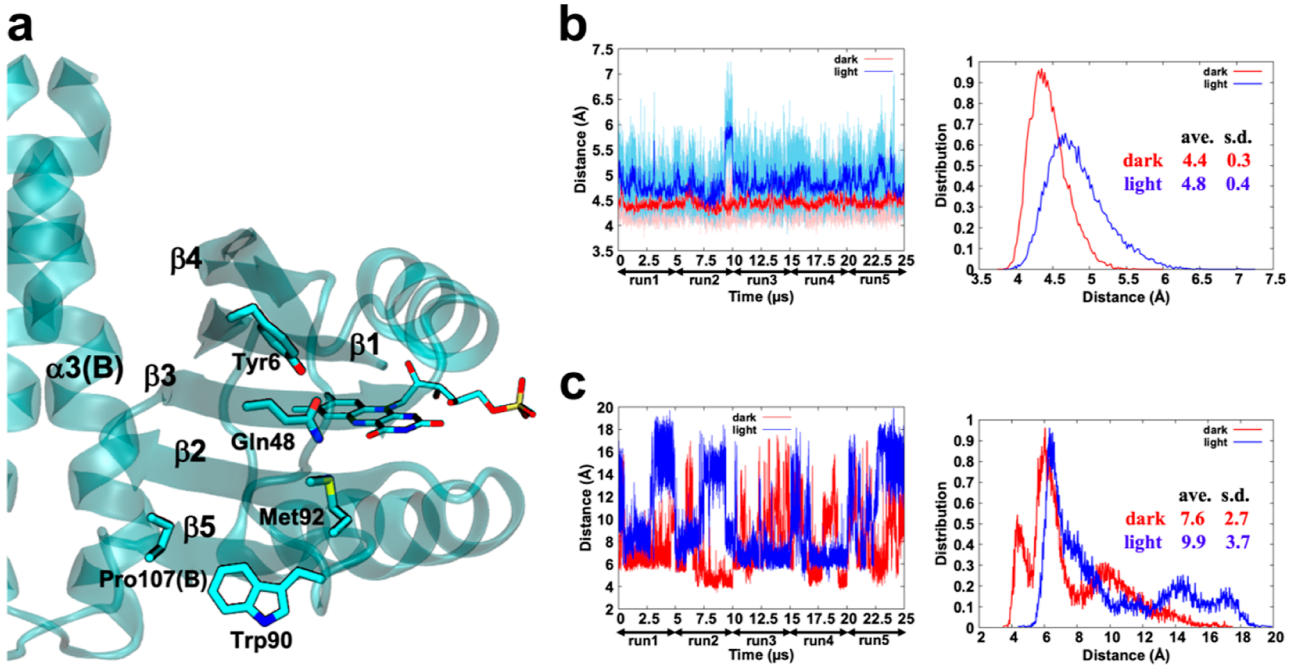

Figure 6. Conformational changes of Met92 and Trp90. (a) Important residues are shown in stick representation. (b) Temporal change of distance between the C_δ atom of Gln48 and the S_δ atom of Met92 and the distribution of the distance are shown. (c) Distance between the center of mass of six carbon atoms in the benzyl part of the indole ring of Trp90 and the center of mass of five atom rings of Pro107(B) and the distribution of the distance are shown. The inset shows the distribution statistics from (b,c); average (ave.) and standard deviation (s.d.) values are given in Å.

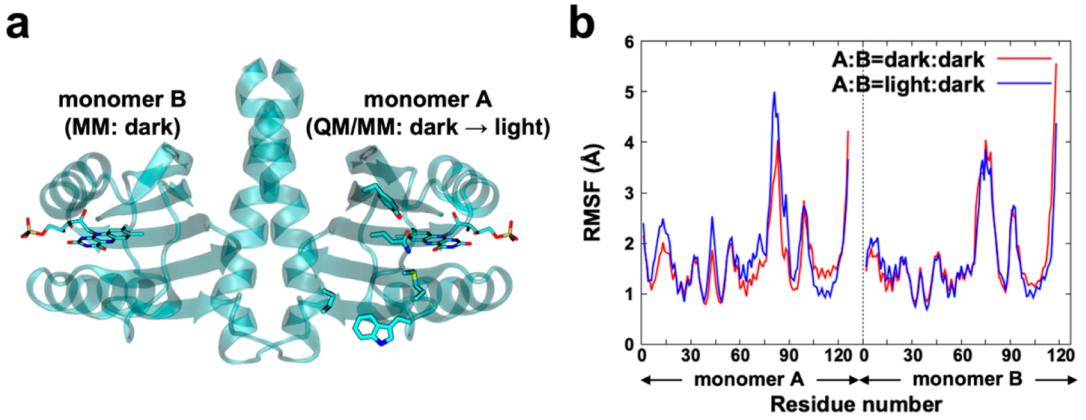

Figure 7. RMSF of BLUF-dimer. (a) Structure of BLUF-dimer is shown. In this study, only monomer A is modeled by QM/MM, while monomer B is treated at the MM level. (b) Residue-wise RMSFs of the dark and light states are shown. The vertical dotted line is a partition between the monomers A and B.

strong hydrogen bonds to the FMN (Figure 4c) but not with Met92, resulting in the dissociation of Met92 from Gln48 (Figure 6a,b).[12] The average distance between the C_δ atom of Gln48 and the S_δ atom of Met92 in the light state (4.8 ± 0.4 Å) was larger than that of the dark state (4.4 ± 0.3 Å) (Figure 6b). Trp90 near Met92 was observed to dissociate from the α3-helix of monomer B in the light state more frequently than in the dark state (Figure 6a,c). Although there are several peaks in the distance distribution between the center of mass of six carbon atoms in the benzyl moiety of the indole ring of Trp90 and the center of mass of five atoms in the ring of Pro107(B), the average of the distance of the light state (9.9 ± 3.7 Å) becomes larger compared with that of the dark state (7.6 ± 2.7 Å), indicating conformational change at the interface between the BLUF core of monomer A and the α3-helix of monomer B (Figure 6c).

Next, we investigated residue-wise RMSF (Figure 7). Note that in the simulation only monomer A was in the light state and treated as QM/MM. In contrast, monomer B was kept in the dark state and treated as MM in this study. In the light state, the RMSF of monomer A increased except for the α3-helix (from Phe103 to The126), in which it decreased (Figure 7b). Especially, the RMSF of the β4-sheet, one-upstreaming from the β5-sheet in which Met92 is located, further increases for the light state. In monomer B, the RMSF is almost the same regardless of monomer A state.

We also evaluated the residue-wise difference contact map between the dark and light states. First, we assessed the residue-wise difference contact map for intramonomer contacts in each monomer. We found that the ten most contacting residue pairs are located in the intracore region of monomer A. In monomer B, we did not observe the significant difference

https://doi.org/10.1021/acsphyschemau.4c00040
ACS Phys. Chem Au 2024, 4, 647−659

a

ranking	residue pair	ratio (SE)
1	I49-M92	0.76 (0.02)
2	E51-M86	0.67 (0.02)
3	T5-K77	0.58 (0.10)
4	L50-M92	0.56 (0.04)
5	L4-K77	0.52 (0.11)

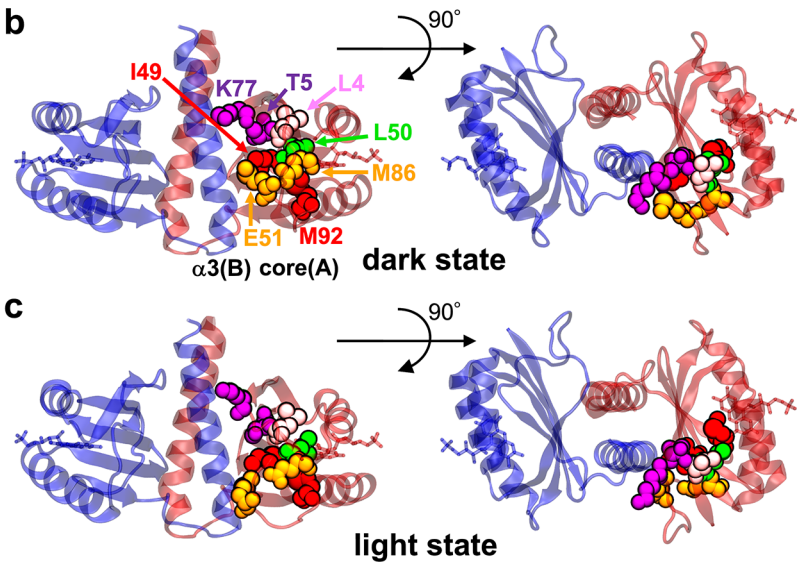

Figure 8. Analysis of residue-wise contacts within monomer A (a) Difference in the contact ratio of the dark and light states. The five most contacted residue pairs in the dark state are listed. Underlined residues appeared twice in the list. Standard error (SE) was calculated from five independent MD runs. (b) Dark-state structure closest to the averaged one over 25 μs trajectories with respect to the backbone atoms. The protein backbone is drawn in ribbon representation. Heavy atoms of the residues listed in (a) are depicted using space-filling model. (c) Light-state structure closest to the averaged one with respect to the backbone atoms.

a

ranking	residue pair	ratio (SE)
1	W90-R106(B)	0.35 (0.15)
2	I95-P107(B)	0.34 (0.07)
3	F87-V110(B)	0.32 (0.09)
4	I49-T114(B)	0.31 (0.16)
5	Q93-F103(B)	0.29 (0.11)

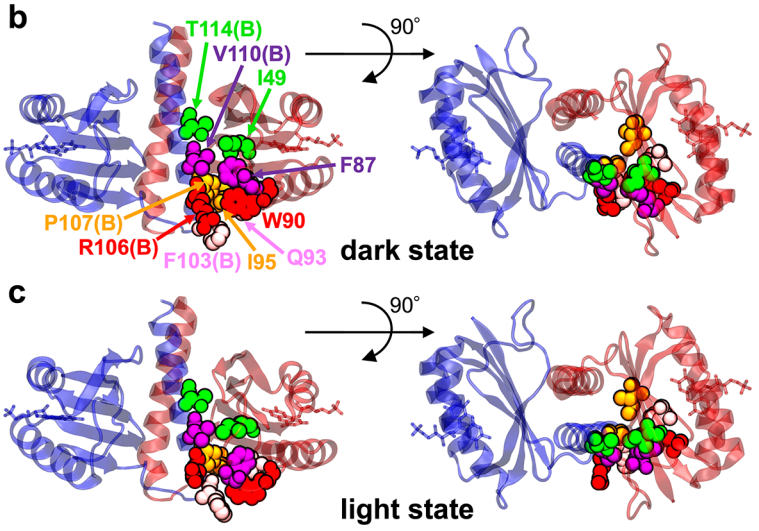

Figure 9. Analysis of residue-wise contacts between monomers A and B. (a) Difference in the contact ratio of the dark and light states. The five most contacted residue pairs in the dark state are listed. Standard error (SE) was calculated from five independent MD runs. (b) Dark-state structure closest to the averaged one over 25 μs trajectories with respect to the backbone atoms. The protein backbone is drawn in ribbon representation. Heavy atoms of the residues listed in (a) are depicted using space-filling model. (c) Light-state structure most closest to the averaged one with respect to the backbone atoms.

between the dark and the light states. Looking into monomer A in the dark and light states, the contact patterns were significantly different between the two states. The ten most contacted residue pairs in the dark state are shown (Figure S3). The residue pairs are primarily seen between the β3-sheet and β5-sheet (Ile49-Met92 and Leu50-Met92), between the β3-sheet and β-hairpin (between the β4-sheet and β5-sheet) (Glu51-Met86 and Glu51-Glu84), and between the β1-sheet and β4-sheet (Thr5-Lys77, Leu4-Lys77, Lys2-Ser78, and Lys2-Glu79) (Figures 8, S1, S3, and S4). Especially, Met92, Ser78, Lys77, Glu51, and Lys2 appeared twice, indicating the importance of these residues for photoactivation. It is noteworthy that Gln48 does not appear in the list, while its neighboring residues, such as Ile49 and Met92, are strongly involved in the interactions, consistent with the fact that Met92 is a key residue for photoactivation pointed out in previous experimental studies[23,24,39] (Figures 8, S3, and S4). Overall, interactions of Met92 and the N-terminal side residues change in the light state. These residue pairs are localized at the boundary between monomers A and B, the core part of monomer A, and the α3-helix of monomer B (Figures 8, S1, S3, and S4).

Second, we evaluated the residue-wise difference contact map between monomers A and B (Figure S5). The ten most contacted residue pairs in the dark state are shown (Figure S5). The residue pairs are observed between the β5-sheet and the

https://doi.org/10.1021/acsphyschemau.4c00040
ACS Phys. Chem Au 2024, 4, 647−659

N-terminus of the α3-helix in monomer B (Ile95-Pro107(B), Gln93-Phe103(B), and Gln93-Pro107(B)) and between the β-hairpin (between the β4-sheet and β5-sheet) and the middle and C-terminus side of the α3-helix in monomer B (Trp90-Arg106(B), Phe87-Val110(B), Asp89-Arg106(B), and Phe87-Arg106(B)) (Figures 9, S1, S5, and S6). Especially, Phe87, Gln93, Arg106(B), and Pro107(B) appeared more than once, indicating the importance of these residues for photoactivation. In addition, the interaction between two α3-helices, Ile105-Leu104(B), was observed. Notably, Trp90, pointed out as important for photoactivation previously,[23,32,36,39,40,66−68] appeared at the top of the list (Figures 9, S5, and S6). Overall, ten top contacting residue pairs are between the core region of monomer A and the α3-helix of monomer B, except for the ninth ranked, Ile105-Leu104(B), which is the interaction between two α3-helices as we mentioned above. No contacting residue pairs appeared between the α3-helix of monomer A and the core region of monomer B. Main interaction differences are localized residue pairs between the core region of monomer A and the α3-helix of monomer B, especially between residues of the β5-sheet of monomer A and the N-terminus of the α3-helix of monomer B (Figures 9, S1, S5, and S6).

Next, we investigated changes in secondary structure (Figures S7 and S8). We did not see a change for monomer B, which was treated as the MM region in both dark and light models. For monomer A, a part of the β4-sheet was lost in the light state. This partial collapse of the strand was consistent with the decrease of the contact ratio of residues between the β1- and β4-sheets (especially Ser78 and Lys77) shown above.

Finally, we compared the angle changes against the α3 helix between the dark and light states (Figure S9). Although the angles between α3(A) and α1(A), between α3(B) and α1(A), and between α3(A) and α3(B) were roughly similar between the dark and light states, some differences in the two former angles were detected, suggesting an orientational change of the α3 helices to the core region of monomer A.

Evaluation of the Absorption Wavelength

We calculated the absorption wavelengths of the dark and light states based on the structures obtained by free-energy optimizations (Table 2). The results of the XMCQDPT2 calculations agree well with the experimental values in the absolute absorption wavelength itself and in the difference of the absorption wavelengths,[10] indicating that the obtained structural models are reasonable.

Table 2. Comparison of the Absorption Wavelength Shift between Our Calculation and Experiment[12] (in nm)

		wavelength	shift
CASSCF	dark-state	362.3	9.8
	light-state	372.1	
XMCQDPT2	dark-state	430.6	12.7
	light-state	443.3	
experiment	dark-state	443.5	9.6
	light-state	453.1	

DISCUSSION AND CONCLUDING REMARKS

As mentioned in the Introduction, there is inconsistency in the Gln48 side chain structures in the light state between the studies based on FTIR experiments[38,41] and the crystallographic structures.[12,13] Our computational study supports that the Gln48 side chain adopts an enolized and rotated conformation in the light state. Moreover, our QM calculations of the enol- and keto-form of Gln in the gas phase clarified that the enol-form is 14.3 kcal/mol more unstable than the keto-form (Table S1).[91] However, the chemically unstable enolized Gln in the protein is stabilized by the hydrogen bonding network of Tyr6 and the chromophore FMN (Figure 4c). Component analysis of the free-energy difference between the dark and light states indicates that only a small part of the total energy gain upon blue light reception is stored in the photoactivated region (QM region, $\Delta_{L2-D}E_{QM}$ = 3.5 kcal/mol) (Table 1). Instead, the energy is primarily stored as the ligand−protein/solvent, solvent−protein, and intraprotein energies, i.e., QM-MM and MM energies, $\Delta_{L2-D}F_{QM-MM,MM}$ = 8.3 kcal/mol (hereafter referred to as environment according to ref 91). This suggests that the protein structure is essential to maintaining a chemically unstable enolized Gln48 in milliseconds to seconds during the photoactive signaling state. A similar exploitation of the environment has been reported in the case of the Mn cluster of photosystem II, where the protein and solvent environment significantly reduces the reactive free energy of the oxidization state and electron transfer reaction.[92] Additionally, our calculations indicate that the light state has 11.8 kcal/mol more energy than the dark state ($\Delta_{L2-D}F_{QM/MM'}$, Table 1). Considering that the free-energy difference evaluated in this study corresponds to that between ground states, the energy of 11.8 kcal/mol is sufficiently smaller than the energy from the absorption of 450 nm blue light of 63.6 kcal/mol. Thus, the energy mostly contributes to the photoexcitation process. Meanwhile, the energy of the light state is also sufficiently high not to be achieved just within the thermal fluctuations, demonstrating the consistency of the present result.

The differences in residue-wise contact maps between the dark and light states show a significant change in Met92 and Trp90, which has been known to be essential for signal transduction.[23,24,32,36,39,40,66−68] Our results show that the Ile49-Met92 pair within monomer A and the Trp90(A)-Arg106(B) pair between monomers A and B are crucial, which can explain the importance of these residues (Figures 8, 9, S3, and S5). In fact, mutations of these residues lead to loss of the signal transduction.[23,24,32,36,39,40,66−68] We showed that contacts with residue pairs between the β3 and β5 sheets, the β3 sheet and β4,5 hairpin, and the β1 and β4 sheets significantly changed between the dark and light states. Among these, Arg77, the third and fifth most significant changes in the intramonomer A contact map, and Thr114, ranked at fourth in the contact map between monomers A and B, are also reported to be important for photoactivation.[13] In addition, a cryotrap experiment detected the structural changes of β4 and β5 sheets and β4,5 hairpin at five seconds after blue light irradiation.[93] Consistently, the contact map differs significantly between the dark and light states in our simulation, suggesting that residue pairs identified as being important for signal transduction by the cryotrap experiment are detected in our study. The cryotrap experiment also clarified the structural differences from Pro88 to Phe103, especially the region from Pro88 to Gln93, which takes an S-shaped form in the dark state and extends to the light state. Still, this was not observed in our simulation.

We found that a part of the β4 sheet region in the dark state was lost in the light state (Figures S7 and S8). The

https://doi.org/10.1021/acsphyschemau.4c00040
ACS Phys. Chem Au 2024, 4, 647−659

conformational change of Met92 (located at β5 sheet) near Gln48 in the light state might be associated with the perturbation of the sheet (Figure 6), and the extension of the β4 sheet locating the N-terminal side of the β5 sheet is induced, although the structure of the C-terminal side, which is considered as important for signal transduction, did not change in the dark and light states. We observed small orientational changes between the BLUF core and the C-terminal helix (Figure S9b,c).

Crystal structure analyses have revealed two distinct conformations of the BLUF domain: $Trp90_{out}$/$Met92_{in}$[10,12−14,18,20,21,23] and $Trp90_{in}$/$Met92_{out}$.[19,22,23] In the case of OaPAC, the cryotrap experiment mentioned above clarified that the $Trp90_{out}$/$Met92_{in}$ conformation corresponds to the dark-state structure, and the $Trp90_{in}$/$Met92_{out}$ conformation corresponds to the light-state structure, respectively.[93] In the cryotrap experiment, the structural transition from the former to the latter conformation occurs within 5 s of light irradiation. Similarly, a recent absorption experiment showed that structural changes of α3 helices, thought to follow the dark-to-light structural transition, occur in the milliseconds order.[67] These structural transitions were not observed in our simulation study, presumably because of the short timescale of simulation (second or millisecond order in experiments vs microsecond order in our simulation). Meanwhile, our study detected Trp90 and Met92 as residues, with the most significant difference in the contact maps. Their fluctuations increased at the light state (Figures 6−8). These changes will eventually lead to a structural transition on a longer timescale. However, the crystallographic structures of OaPAC and bPAC keep the $Trp90_{out}$/$Met92_{in}$ conformation after several tens of seconds after blue-light irradiation,[12,13] indicating that crystal packing may prevent structural changes.

Recently, the deactivation of two BLUF proteins, BlrB and AppA, was studied with a hybrid QM/MM simulation to understand the wide span of dark-state recovery times.[94] In that study, the intermediate states between the light and dark states were explicitly considered using a path-constrained MD, indicating that the conformation of Trp and Gln near FAD is important in modulating the recovery time. Our study focused on the conformational differences between the dark and light states using the free-energy optimized BLUF structures rather than focusing on the transition states. Our approach, although limited to dealing with the end structures of the dark and light states without addressing the intermediate states, clarified significant changes in residue-wise contacts between intrachain residues and those between interchain residues (Figures 8 and 9), indicating the importance of the residues. In addition, we showed that the light-absorption energy is more distributed to the surrounding residues around FAD than stored in Tyr-Gln-FAD. These results will help us to understand the signal transition from the BLUF domain to the AC domain of OaPAC.

Nakasone et al. showed by the transient grating method that the structural change of the dimer consisting of two light-state monomers was more than double what was expected from the dimer consisting of one dark and one light monomers, suggesting a nonlinear increase of structural change as dimer upon blue light reception.[68] Also, they proposed that a relative orientational change between the BLUF domain and the AC domain via the α3 helices is necessary for signal transduction. Currently, we are working on molecular simulations of full-length OaPAC to get insights into how photoactivation of the BLUF domain regulates the catalytic activity in the AC domain, which will be reported elsewhere. Moreover, the rational design of mutant proteins with a desired wavelength shifting from the wild type would be possible by a systematic physicochemical analysis using the QM/MM free-energy method, which was used for one of the model structure validations in the present study.

■ ASSOCIATED CONTENT

Data Availability Statement

Coordinate data of the free energetically optimized structures of the QM region for all the states obtained in the present study are included in Supporting Information. See Methods for detailed descriptions of the software along with workflows and parameter setting of the simulations. The codes for the QM/MM RWFE-SCF calculation used in the present study are available through the developed group[64] upon request.

Supporting Information

The Supporting Information is available free of charge at https://pubs.acs.org/doi/10.1021/acsphyschemau.4c00040.

An amino acid sequence of the BLUF domain used in this study, quantum mechanically treated regions in the QM/MM RWFE-SCF calculations, energy difference between the keto and enol structures of Gln in the gas phase, analysis of residue-wise different contact map between the dark and light states, analysis of secondary structure changes for the dark and light states, analysis of orientational changes of the long C-terminal helices for the dark and light states, and absolute energy values of QM components (PDF)

Coordinate data of the optimized structure in the dark, light 1, and light 2 states (ZIP)

■ AUTHOR INFORMATION

Corresponding Author

Hidetoshi Kono − *Institute for Quantum Life Science, National Institutes for Quantum Science and Technology, Chiba 263-8555, Japan; Graduate School of Science and Engineering, Chiba University, Chiba 263-8522, Japan;* orcid.org/0000-0001-5729-8707; Phone: +81-43-382-4295; Email: kono.hidetoshi@qst.go.jp

Authors

Masahiko Taguchi − *Institute for Quantum Life Science, National Institutes for Quantum Science and Technology, Chiba 263-8555, Japan; Institute of Multidisciplinary Research for Advanced Materials, Tohoku University, Sendai 980-8577, Japan*

Shun Sakuraba − *Institute for Quantum Life Science, National Institutes for Quantum Science and Technology, Chiba 263-8555, Japan; Graduate School of Science and Engineering, Chiba University, Chiba 263-8522, Japan;* orcid.org/0000-0001-5768-2389

Justin Chan − *Institute for Quantum Life Science, National Institutes for Quantum Science and Technology, Chiba 263-8555, Japan*

Complete contact information is available at: https://pubs.acs.org/10.1021/acsphyschemau.4c00040

Notes

The authors declare no competing financial interest.

https://doi.org/10.1021/acsphyschemau.4c00040
ACS Phys. Chem Au 2024, 4, 647−659

■ ACKNOWLEDGMENTS

We thank Kiharu Abe, Takafumi Shikakura, Motoshi Kamiya, Taisuke Hasegawa, Daichi Yamada, Yusuke Nakasone, Shigehiko Hayashi, Mitsunori Ikeguchi, and Sam-Yong Park for valuable discussions and comments. Molecular figures were created using visual molecular dynamics (VMD).[95] This work was supported by JSPS KAKENHI (grant no. 23K14139), MEXT Q-LEAP (grant no. JPMXS0120330644), and AMED BINDS (grant no. 24ama121024j0003). Some computations were performed at the Research Center for Computational Science, Okazaki, Japan (Project ID: 21-IMS-C128 and 22-IMS-C126). Also, some computations were performed using the HPE-SGI8600 supercomputer provided by National Institutes for Quantum Science and Technology and Japan Atomic Energy Agency.

■ REFERENCES

(1) Zhou, Z.; Tanaka, K. F.; Matsunaga, S.; Iseki, M.; Watanabe, M.; Matsuki, N.; Ikegaya, Y.; Koyama, R. Photoactivated adenylyl cyclase (PAC) reveals novel mechanisms underlying cAMP-dependent axonal morphogenesis. *Sci. Rep.* **2016**, *6*, 19679.

(2) Qi, C.; Sorrentino, S.; Medalia, O.; Korkhov, V. M. The structure of a membrane adenylyl cyclase bound to an activated stimulatory G protein. *Science* **2019**, *364*, 389−394.

(3) Iseki, M.; Matsunaga, S.; Murakami, A.; Ohno, K.; Shiga, K.; Yoshida, K.; Sugai, M.; Takahashi, T.; Hori, T.; Watanabe, M. A blue-light-activated adenylyl cyclase mediates photoavoidance in *Euglena gracilis*. *Nature* **2002**, *415*, 1047−1051.

(4) Jansen, V.; Alvarez, L.; Balbach, M.; Strünker, T.; Hegemann, P.; Kaupp, U. B.; Wachten, D. Controlling fertilization and cAMP signaling in sperm by optogenetics. *eLife* **2015**, *4*, No. e05161.

(5) Kinjo, T.; Watabe, T.; Kobachi, K.; Terai, K.; Matsuda, M. Single-Cell Activation of the cAMP-Signaling Pathway in 3D Tissues with FRET-Assisted Two-Photon Activation of bPAC. *ACS Chem. Biol.* **2020**, *15*, 2848−2853.

(6) Xia, A.; Qian, M.; Congcong, W.; Huang, Y.; Liu, Z.; Ni, L.; Jin, F. Optogenetic Modificaion of Prseudomonas aeruginosa Enables Controllable Twitching Motility and Host Infection. *ACS Synth. Biol.* **2021**, *10*, 531−541.

(7) Iseki, M.; Park, S.-Y. Photoactivated Adenylyl Cyclases: Fundamental Properties and Applications. *Adv. Exp. Med. Biol.* **2021**, *1293*, 129−139.

(8) Hansen, J. N.; Kaiser, F.; Leyendecker, P.; Stüven, B.; Krause, J.-H.; Derakhshandeh, F.; Irfan, J.; Sroka, T. J.; Preval, K. M.; Desai, P. B.; Kraut, M.; Theis, H.; Drews, A.-D.; De-Domenico, E.; Händler, K.; Pazour, G. J.; Henderson, D. J. P.; Mick, D. U.; Wachten, D. A cAMP signalosome in primary cilia drives gene expression and kidney cyst formation. *EMBO Rep.* **2022**, *23*, No. e54315.

(9) Stierl, M.; Penzkofer, A.; Kennis, J. T. M.; Hegemann, P.; Mathes, T. Key Residues for the Light Regulation of the Blue Light-Activated Adenylyl Cyclase from *Beggiatoa* sp. *Biochemistry* **2014**, *53*, 5121−5130.

(10) Ohki, M.; Sugiyama, K.; Kawai, F.; Tanaka, H.; Nihei, Y.; Unzai, S.; Takebe, M.; Matsunaga, S.; Adachi, S.; Shibayama, N.; Zhou, Z.; Koyama, R.; Ikegaya, Y.; Takahashi, T.; Tame, J. R. H.; Iseki, M.; Park, S.-Y. Structural insight into photoactivation of an adenylate cyclase from a photosynthetic cyanobacterium. *Proc. Natl. Acad. Sci. U.S.A.* **2016**, *113*, 6659−6664.

(11) Yang, S.; Constantin, O. M.; Sachidanandan, D.; Hofmann, H.; Kunz, T. C.; Kozjak-Pavlovic, V.; Oertner, T. G.; Nagel, G.; Kittel, R. J.; Gee, C. E.; Gao, S. PACmn for improved optogenetic control of intracellular cAMP. *BMC Biol.* **2021**, *19*, 227.

(12) Ohki, M.; Sato-Tomita, A.; Matsunaga, S.; Iseki, M.; Tame, J. R. H.; Shibayama, N.; Park, S.-Y. Molecular mechanism of photoactivation of a light-regulated adenylate cyclase. *Proc. Natl. Acad. Sci. U.S.A.* **2017**, *114*, 8562−8567.

(13) Lindner, R.; Hartmann, E.; Tarnawski, M.; Winkler, A.; Frey, D.; Reinstein, J.; Meinhart, A.; Schlichting, I. Photoactivation Mechanism of a Bacterial Light-Regulated Adenylyl Cyclase. *J. Mol. Biol.* **2017**, *429*, 1336−1351.

(14) Barends, T. R.; Hartmann, E.; Griese, J. J.; Beitlich, T.; Kirienko, N. V.; Ryjenkov, D. A.; Reinstein, J.; Shoeman, R. L.; Gomelsky, M.; Schlichting, I. Structure and mechanism of a bacterial light-regulated cyclic nucleotide phosphodiesterase. *Nature* **2009**, *459*, 1015−1018.

(15) Masuda, S.; Bauer, C. E. AppA Is a Blue Light Photoreceptor that Antirepresses Photosynthesis Gene Expression in *Rhodobacter sphaeroides*. *Cell* **2002**, *110*, 613−623.

(16) Möglich, A.; Yang, X.; Ayers, R. A.; Moffat, K. Structure and Function of Plant Photoreceptors. *Annu. Rev. Plant Biol.* **2010**, *61*, 21−47.

(17) Kennis, J. T. M.; Mathes, T. Molecular eyes: proteins that transform light into biological information. *Interface Focus* **2013**, *3*, 20130005.

(18) Kita, A.; Okajima, K.; Morimoto, Y.; Ikeuchi, M.; Miki, K. Structure of a Cyanobacterial BLUF Protein, Tll0078, Containing a Novel FAD-binding Blue Light Sensor Domain. *J. Mol. Biol.* **2005**, *349*, 1−9.

(19) Anderson, S.; Dragnea, V.; Masuda, S.; Ybe, J.; Moffat, K.; Bauer, C. Structure of a Novel Photoreceptor, the BLUF Domain of AppA from *Rhodobacter sphaeroides*. *Biochemistry* **2005**, *44*, 7998−8005.

(20) Jung, A.; Domratcheva, T.; Tarutina, M.; Wu, Q.; Ko, W.-H.; Shoeman, R. L.; Gomelsky, M.; Gardner, K. H.; Schlichting, I. Structure of a bacterial BLUF photoreceptor: Insights into blue light-mediated signal transduction. *Proc. Natl. Acad. Sci. U.S.A.* **2005**, *102*, 12350−12355.

(21) Jung, A.; Reinstein, J.; Domracheva, T.; Shoeman, R. L.; Schlichting, I. Crystal Structures of the AppA BLUF Domain Photoreceptor Provide Insights into Blue Light-mediated Signal Transduction. *J. Mol. Biol.* **2006**, *362*, 717−732.

(22) Grinstead, J. S.; Hsu, S.-T. D.; Laan, W.; Bonvin, A. M. J. J.; Hellingwerf, K. J.; Boelens, R.; Kaptein, R. The Solution Structure of the AppA BLUF Domain: Insight into the Mechanism of Light-Induced Signaling. *Chembiochem* **2006**, *7*, 187−193.

(23) Yuan, H.; Anderson, S.; Masuda, S.; Dragnea, V.; Moffat, K.; Bauer, C. Crystal Structures of the Synechocystis Photoreceptor Slr1694 Reveal Distinct Structural States Related to Signaling. *Biochemistry* **2006**, *45*, 12687−12694.

(24) Wu, Q.; Gardner, K. H. Structure and Insight into Blue Light-Induced Changes in the BlrP1 BLUF Domain. *Biochemistry* **2009**, *48*, 2620−2629.

(25) Kraft, B. J.; Masuda, S.; Kikuchi, J.; Dragnea, V.; Tollin, G.; Zaleski, J. M.; Bauer, C. E. Spectroscopic and Mutational Analysis of the Blue-Light Photoreceptor AppA: A Novel Photocycle Involving Flavin Stacking with an Aromatic Amino Acid. *Biochemistry* **2003**, *42*, 6726−6734.

(26) Masuda, S.; Hasegawa, K.; Ishii, A.; Ono, T. Light-Induced Structural Changes in a Putative Blue-Light Receptor with a Novel FAD Binding Fold Sensor of Blue-Light Using FAD (BLUF); Slr1694 of *Synechocystis* sp. PCC6803. *Biochemistry* **2004**, *43*, 5304−5313.

(27) Hasegawa, K.; Masuda, S.; Ono, T. Structural Intermediate in the Photocycle of a BLUF (Sensor of Blue Light Using FAD) Protein Slr1694 in a Cyanobacterium *Synechocystis* sp. PCC6803. *Biochemistry* **2004**, *43*, 14979−14986.

(28) Masuda, S.; Hasegawa, K.; Ono, T. Light-Induced Structural Changes of Apoprotein and Chromophore in the Sensor of Blue Light Using FAD (BLUF) domain of AppA for a Signaling State. *Biochemistry* **2005**, *44*, 1215−1224.

(29) Dragnea, V.; Waegele, M.; Balascuta, S.; Bauer, C.; Dragnea, B. Time-Resolved Spectroscopic Studies of the AppA Blue-Light Receptor BLUF Domain from *Rhodobacter sphaeroides*. *Biochemistry* **2005**, *44*, 15978−15985.

(30) Gauden, M.; van Stokkum, I. H. M.; Key, J. M.; Lührs, D. C.; van Grondelle, R.; Hegemann, P.; Kennis, J. T. M. Hydrogen-bond

switching through a radical pair mechanism in a flavin-binding photoreceptor. *Proc. Natl. Acad. Sci. U.S.A.* **2006**, *103*, 10895−10900.
(31) Unno, M.; Masuda, S.; Ono, T.; Yamauchi, S. Orientation of a Key Glutamine Residue in the BLUF Domain from AppA Revealed by Mutagenesis, Spectroscopy, and Quantum Chemical Calculations. *J. Am. Chem. Soc.* **2006**, *128*, 5638−5639.
(32) Stelling, A. L.; Ronayne, K. L.; Nappa, J.; Tonge, P. J.; Meech, S. R. Ultrafast Structural Dynamics in BLUF Domains: Transient Infrared Spectroscopy of AppA and Its Mutants. *J. Am. Chem. Soc.* **2007**, *129*, 15556−15564.
(33) Lukacs, A.; Haigney, A.; Brust, R.; Zhao, R.-K.; Stelling, A. L.; Clark, I. P.; Towrie, M.; Greetham, G. M.; Meech, S. R.; Tonge, P. J. Photoexcitation of the Blue Light Using FAD Photoreceptor AppA Results in Ultrafast Changes to the Protein Matrix. *J. Am. Chem. Soc.* **2011**, *133*, 16893−16900.
(34) Iwata, T.; Watanabe, A.; Iseki, M.; Watanabe, M.; Kandori, H. Strong Donation of the Hydrogen Bond of Tyrosine during Photoactivation of the BLUF Domain. *J. Phys. Chem. Lett.* **2011**, *2*, 1015−1019.
(35) Lukacs, A.; Brust, R.; Haigney, A.; Laptenok, S. P.; Addison, K.; Gil, A.; Towrie, M.; Greetham, G. M.; Tonge, P. J.; Meech, S. R. BLUF Domain Function Does Not Require a Metastable Radical Intermediate State. *J. Am. Chem. Soc.* **2014**, *136*, 4605−4615.
(36) Mehlhorn, J.; Lindtner, T.; Richter, F.; Glaß, K.; Steinocher, H.; Beck, S.; Hegemann, P.; Kennis, J. T. M.; Mathes, T. Light-Induced Rearrangement of the β5 Strand in the BLUF Photoreceptor SyPixD (Slr1694). *J. Phys. Chem. Lett.* **2015**, *6*, 4749−4753.
(37) Domratcheva, T.; Hartmann, E.; Schlichting, I.; Kottke, T. Evidence for Tautomerisation of Glutamine in BLUF Blue Light Receptors by Vibrational Spectroscopy and Computational Chemistry. *Sci. Rep.* **2016**, *6*, 22669.
(38) Iwata, T.; Nagai, T.; Ito, S.; Osoegawa, S.; Iseki, M.; Watanabe, M.; Unno, M.; Kitagawa, S.; Kandori, H. Hydrogen Bonding Environments in the Photocycle Process around the Flavin Chromophore of the AppA-BLUF domain. *J. Am. Chem. Soc.* **2018**, *140*, 11982−11991.
(39) Hall, C. R.; Tolentino Collado, J.; Iuliano, J. N.; Gil, A. A.; Adamczyk, K.; Lukacs, A.; Greetham, G. M.; Sazanovich, I.; Tonge, P. J.; Meech, S. R. Site-Specific Protein Dynamics Probed by Ultrafast Infrared Spectroscopy of a Noncanonical Amino Acid. *J. Phys. Chem. B* **2019**, *123*, 9592−9597.
(40) Tolentino Collado, J.; Iuliano, J. N.; Pirisi, K.; Jewlikar, S.; Adamczyk, K.; Greetham, G. M.; Towrie, M.; Tame, J. R. H.; Meech, S. R.; Tonge, P. J.; Lukacs, A. Unraveling the Photoactivation Mechanism of a Light-Activated Adenylyl Cyclase Using Ultrafast Spectroscopy Coupled with Unnatural Amino Acid Mutagenesis. *ACS Chem. Biol.* **2022**, *17*, 2643−2654.
(41) Hontani, Y.; Mehlhorn, J.; Domratcheva, T.; Beck, S.; Kloz, M.; Hegemann, P.; Mathes, T.; Kennis, J. T. M. Spectroscopic and Computational Observation of Glutamine Tautomerization in the Blue Light Sensing Using Flavin Domain Photoreaction. *J. Am. Chem. Soc.* **2023**, *145*, 1040−1052.
(42) Collado, J. T.; Bodis, E.; Pasitka, J.; Szucs, M.; Fekete, Z.; Kis-Bicskei, N.; Telek, E.; Pozsonyi, K.; Kapetanaki, S. M.; Greetham, G.; Tonge, P. J.; Meech, S. R.; Lukacs, A. Single Amino Acid Mutation Decouples Photochemistry of the BLUF Domain from the Enzymatic Function of OaPAC and Drives the Enzyme to a Switched-on State. *J. Mol. Biol.* **2024**, *436*, 168312.
(43) Domratcheva, T.; Grigorenko, B. L.; Schlichting, I.; Nemukhin, V. Molecular Models Predict Light-Induced Glutamine Tautomerization in BLUF Photoreceptors. *Biophys. J.* **2008**, *94*, 3872−3879.
(44) Sadeghian, K.; Bocola, M.; Schütz, M. A Conclusive Mechanism of the Photoinduced Reaction Cascade in Blue Light Using Flavin Photoreceptors. *J. Am. Chem. Soc.* **2008**, *130*, 12501−12513.
(45) Obanayama, K.; Kobayashi, H.; Fukushima, K.; Sakurai, M. Structures of the Chromophore Binding Sites in BLUF Domains as Studied by Molecular Dynamics and Quantum Chemical Calculations. *Photochem. Photobiol.* **2008**, *84*, 1003−1010.
(46) Götze, J.; Saalfrank, P. Serine in BLUF domains displays spectral importance in computational models. *J. Photochem. Photobiol., B* **2009**, *94*, 87−95.
(47) Khrenova, M. G.; Nemukhin, A. V.; Grigorenko, B. L.; Krylov, A. I.; Domratcheva, T. M. Quantum Chemistry Calculations Provide Support to the Mechanism of the Light-Induced Structural Changes in the Flavin-Binding Photoreceptor Proteins. *J. Chem. Theory Comput.* **2010**, *6*, 2293−2302.
(48) Sadeghian, K.; Bocola, M.; Schütz, M. A QM/MM study on the fast photocycle of blue light using flavin photoreceptors in their light-adapted/active form. *Phys. Chem. Chem. Phys.* **2010**, *12*, 8840−8846.
(49) Rieff, B.; Bauer, S.; Mathias, G.; Tavan, P. DFT/MM Description of Flavin IR Spectra in BLUF Domains. *J. Phys. Chem. B* **2011**, *115*, 11239−11253.
(50) Merz, T.; Sadeghian, K.; Schütz, M. Why BLUF photoreceptor with roseoflavin cofactors lose their biological functionality. *Phys. Chem. Chem. Phys.* **2011**, *13*, 14775−14783.
(51) Udvarhelyi, A.; Domracheva, T. Photoreaction in BLUF Receptors: Proton-coupled Electron Transfer in the Flavin-Gln-Tyr System. *Photochem. Photobiol.* **2011**, *87*, 554−563.
(52) Hisao, Y.-W.; Götze, J. P.; Thiel, W. The Central Role of Gln63 for the Hydrogen Bonding Network and UV-Visible Spectrum of the AppA BLUF Domain. *J. Phys. Chem. B* **2012**, *116*, 8064−8073.
(53) Khrenova, M. G.; Nemukhin, A. V.; Domracheva, T. Photoinduced Electron Transfer Facilitates Tautomerization of the Conserved Signaling Glutamine Side Chain in BLUF Protein Light Sensors. *J. Phys. Chem. B* **2013**, *177*, 2369−2377.
(54) Udvarhelyi, A.; Domracheva, T. Glutamine Rotamors in BLUF Photoreceptors: A Mechanistic Reappraisal. *J. Phys. Chem. B* **2013**, *117*, 2888−2897.
(55) Collette, F.; Renger, T.; Schmidt am Busch, M. Revealing the Functional States in the Active Site of BLUF Photoreceptors from Electrochromic Shift Calculations. *J. Phys. Chem. B* **2014**, *118*, 11109−11119.
(56) Udvarhelyi, A.; Olivucci, M.; Domratcheva, T. Role of the Molecular Environment in Flavoprotein Color and Redox Tuning: QM Cluster versus QM/MM Modeling. *J. Chem. Theory Comput.* **2015**, *11*, 3878−3894.
(57) Goyal, P.; Hammes-Schiffer, S. Role of Active Site Conformational Changes in Photocycle Activation of the AppA BLUF Photoreceptor. *Proc. Natl. Acad. Sci. U.S.A.* **2017**, *114*, 1480−1485.
(58) Goings, J. J.; Reinhardt, C. R.; Hammes-Schiffer, S. Propensity for Proton Relay and Electrostatic Impact of Protein Reorganization in Slr1694 BLUF Photoreceptor. *J. Am. Chem. Soc.* **2018**, *140*, 15241−15251.
(59) Sayfutyarova, E. R.; Goings, J. J.; Hammes-Schiffer, S. Electron-Coupled Double Proton Transfer in the Slr1694 BLUF Photoreceptor: A Multireference Electronic Structure Study. *J. Phys. Chem. B* **2019**, *123*, 439−447.
(60) Goings, J. J.; Hammes-Schiffer, S. Early Photocycle of Slr1694 Blue-Light Using Flavin Photoreceptor Unraveled through Adiabatic Excited-State Quantum Mechanical/Molecular Mechanical Dynamics. *J. Am. Chem. Soc.* **2019**, *141*, 20470−20479.
(61) Goings, J. J.; Li, P.; Zhu, Q.; Hammes-Schiffer, S. Formation of an Unusual Glutamine Tautomer in a Blue Light Using Flavin Photocycle Characterizes the Light-Adapted State. *Proc. Natl. Acad. Sci. U.S.A.* **2020**, *117*, 26626−26632.
(62) Hashem, S.; Macaluso, V.; Nottoli, M.; Lipparini, F.; Cupellini, L.; Mennucci, B. From crystallographic data to the solution structure of photoreceptors: the case of the AppA BLUF domain. *Chem. Sci.* **2021**, *12*, 13331−13342.
(63) Kosugi, T.; Hayashi, S. QM/MM Reweighting Free Energy SCF for Geometry Optimization on Extensive Free Energy Surface of Enzymatic Reaction. *J. Chem. Theory Comput.* **2012**, *8*, 322−334.
(64) Hayashi, S.; Uchida, Y.; Hasegawa, T.; Higashi, M.; Kosugi, T.; Kamiya, M. QM/MM Geometry Optimization on Extensive Free-Energy Surfaces for Examination of Enzymatic Reactions and Design of Novel Functional Properties of Proteins. *Annu. Rev. Phys. Chem.* **2017**, *68*, 135−154.

https://doi.org/10.1021/acsphyschemau.4c00040
ACS Phys. Chem Au 2024, 4, 647−659

(65) Kosugi, T.; Hayashi, S. Crucial Role of Protein Flexibility in Formation of a Stable Reaction Transition State in an α-Amylase Catalysis. *J. Am. Chem. Soc.* **2012**, *134*, 7045−7055.
(66) Shibata, K.; Nakasone, Y.; Terazima, M. Selective Photo-induced Dimerization and Slow Recovery of a BLUF Domain of EB1. *J. Phys. Chem. B* **2022**, *126*, 1024−1033.
(67) Tokonami, S.; Onose, M.; Nakasone, Y.; Terazima, M. Slow Conformational Changes of Blue Light Sensor BLUF Proteins in Milliseconds. *J. Am. Chem. Soc.* **2022**, *144*, 4080−4090.
(68) Nakasone, Y.; Murakami, H.; Tokunami, S.; Oda, T.; Terzazima, M. Time-resolved study on signalizing pathway of photoactivated adenylate cyclase and its nonlinear optical response. *J. Biol. Chem.* **2023**, *299*, 105285.
(69) Case, D. A.; Ben-Shalom, I. Y.; Brozell, S. R.; Cerutti, D. S.; Cheatham, T. E., III; Cruzeiro, V. W. D.; Darden, T. A.; Duke, R. E.; Ghoreishi, D.; Gilson, M. K.; Gohlke, H.; Goetz, A. W.; Greene, D.; Harris, R.; Homeyer, N.; Huang, Y.; Izadi, S.; Kovalenko, A.; Kurtzman, T.; Lee, T. S.; LeGrand, S.; Li, P.; Lin, C.; Liu, J.; Luchko, T.; Luo, R.; Mermelstein, D. J.; Merz, K. M.; Miao, Y.; Monard, G.; Nguyen, C.; Nguyen, H.; Omelyan, I.; Onufriev, A.; Pan, F.; Qi, R.; Roe, D. R.; Roitberg, A.; Sagui, C.; Schott-Verdugo, S.; Shen, J.; Simmerling, C. L.; Smith, J.; Salomon-Ferrer, R.; Swails, J.; Walker, R. C.; Wang, J.; Wei, H.; Wolf, R. M.; Wu, X.; Xiao, L.; York, D. M.; Kollman, P. A. *AMBER 2018*; University of California: San Francisco, 2018.
(70) Jorgensen, W. L.; Chandrasekhar, J.; Madura, J. D.; Impey, R. W.; Klein, M. L. Comparison of simple potential functions for simulating liquid water. *J. Chem. Phys.* **1983**, *79*, 926−935.
(71) Maier, J. A.; Martinez, C.; Kasavajhala, K.; Wickstrom, L.; Hauser, K. E.; Simmerling, C. ff14SB: Improving the Accuracy of Protein Side Chain and Backbone Parameters from ff99SB. *J. Chem. Theory Comput.* **2015**, *11*, 3696−3713.
(72) Joung, I. S.; Cheatham, T. E., III Determination of Alkali and Halide Monovalent Ion Parameters for Use in Explicitly Solvated Biomolecular Simulations. *J. Phys. Chem. B* **2008**, *112*, 9020−9041.
(73) Becke, A. D. Density-functional thermochemistry. III. The role of exact exchange. *J. Chem. Phys.* **1993**, *98*, 5648−5652.
(74) Grimme, S.; Antony, J.; Ehrlich, S.; Krieg, H. A consistent and accurate *ab initio* parametrization of density functional dispersion correction (DFT-D) for the 94 elements H-Pu. *J. Chem. Phys.* **2010**, *132*, 154104.
(75) Tomasi, J.; Mennucci, B.; Cammi, R. Quantum Mechanical Continuum Solvation Models. *Chem. Rev.* **2005**, *105*, 2999−3094.
(76) Schmidt, M. W.; Baldridge, K. K.; Boatz, J. A.; Elbert, S. T.; Gordon, M. S.; Jensen, J. H.; Koseki, S.; Matsunaga, N.; Nguyen, K. A.; Su, S.; Windus, T. L.; Dupuis, M.; Montgomery, J. A., Jr General atomic and molecular electronic structure system. *J. Comput. Chem.* **1993**, *14*, 1347−1363.
(77) Salomon-Ferrer, R.; Götz, A. W.; Poole, D.; Le Grand, S.; Walker, R. C. Routine Microsecond Molecular Dynamics Simulations with AMBER on GPUs. 2. Explicit Solvent Particle Mesh Ewald. *J. Chem. Theory Comput.* **2013**, *9*, 3878−3888.
(78) Ryckaert, J.-P.; Ciccotti, G.; Berendsen, H. J. C. Numerical Integration of the Cartesian Equations of Motion of a System with Constraints: Molecular Dynamics of *n*-Alkanes. *J. Comput. Phys.* **1977**, *23*, 327−341.
(79) Andersen, H. C. Rattle: A "velocity" version of the shake algorithm for molecular dynamics calculations. *J. Comput. Phys.* **1983**, *52*, 24−34.
(80) Darden, T.; York, D.; Pedersen, L. Particle mesh Ewald: An N·log(N) method for Ewald sums in large systems. *J. Chem. Phys.* **1993**, *98*, 10089−10092.
(81) Berendsen, H. J. C.; Postma, J. P. M.; van Gunsteren, W. F.; DiNola, A.; Haak, J. R. Molecular dynamics with coupling to an external bath. *J. Chem. Phys.* **1984**, *81*, 3684−3690.
(82) Hayashi, S.; Ohmine, I. Proton Transfer in Bacteriorhodopsin: Structure, Excitation, IR Spectra, and Potential Energy Surface Analyses by an ab Initio QM/MM Method. *J. Phys. Chem. B* **2000**, *104*, 10678−10691.
(83) Bennett, C. H. Efficient Estimation of Free Energy Differences from Monte Carlo Data. *J. Comput. Phys.* **1976**, *22*, 245−268.
(84) Shirts, M. R.; Bair, E.; Hooker, G.; Pande, V. S. Equilibrium Free Energies from Nonequilibrium Measurements Using Maximum-Likelihood Methods. *Phys. Rev. Lett.* **2003**, *91*, 140601.
(85) Shirts, M. R.; Pande, V. S. Comparison of efficiency and bias of free energies computed by exponential averaging, the Bennett acceptance ratio, and thermodynamic integration. *J. Chem. Phys.* **2005**, *122*, 144107.
(86) Johnson, R. D., III. NIST Computational Chemistry Comparison and Benchmark Database. https://cccbdb.nist.gov/vibscalejust.asp (accessed Mar 9, 2022).
(87) McGibbon, R. T.; Beauchamp, K. A.; Harrigan, M. P.; Klein, C.; Swails, J. M.; Hernández, C.; Schwantes, C. R.; Wang, L.-P.; Lane, T. J.; Pande, V. S. MDTraj: A Modern Open Library for the Analysis of Molecular Dynamics Trajectories. *Biophys. J.* **2015**, *109*, 1528−1532.
(88) Roe, D. R.; Cheatham, T. E., III PTRAJ and CPPTRAJ: Software for Processing and Analysis of Molecular Dynamics Trajectory Data. *J. Chem. Theory Comput.* **2013**, *9*, 3084−3095.
(89) Nakano, H. Quasidegenerate Perturbation Theory with Multiconfigurational Self-consistent-field Reference Functions. *J. Chem. Phys.* **1993**, *99*, 7983−7992.
(90) Granovsky, A. A. Extended Multi-configuration Quasi-degenerate Perturbation Theory: The New Approach to Multi-state Multi-reference Perturbation Theory. *J. Chem. Phys.* **2011**, *134*, 214113.
(91) Grigorenko, B. L.; Khrenova, M. G.; Nemukhin, A. V. Amide-imide tautomerization in the glutamine side chain in enzymatic and photochemical reactions in proteins. *Phys. Chem. Chem. Phys.* **2018**, *20*, 23827−23836.
(92) Takahashi, H.; Suzuoka, D.; Sakuraba, S.; Morita, A. Role of the Photosystem II as an Environment in the Oxidation Free Energy of an Mn Cluster from S_1 to S_2. *J. Phys. Chem. B* **2019**, *123*, 7081−7091.
(93) Chretien, A.; Nagel, M. F.; Botha, S.; de Wijn, R.; Brings, L.; Dörner, K.; Han, H.; Koliyadu, J. C. P.; Letrun, R.; Round, A.; Sato, T.; Schmidt, C.; Secareanu, R.-C.; von Stetten, D.; Vakili, M.; Wrona, A.; Bean, R.; Mancuso, A.; Schulz, J.; Pearson, A. R.; Kottke, T.; Lorenzen, K.; Schubert, R. Light-induced Trp_{in}/Met_{out} switching during BLUF domain activation in ATP-bound photoactivatable adenylate cyclase OaPAC. *J. Mol. Biol.* **2024**, *436*, 168439.
(94) Oríz, A. P. d. A.; Rovira, C.; Ensing, B. Free energies of the Gln tautomerization and rotation mechanism of dark-state recovery in blue light-using flavin proteins. *bioRxiv* **2023**, 2023.08.11.551373.
(95) Humphrey, W.; Dalke, A.; Schulten, K. VMD: visual molecular dynamics. *J. Mol. Graphics* **1996**, *14*, 33−38.

https://doi.org/10.1021/acsphyschemau.4c00040
ACS Phys. Chem Au 2024, 4, 647−659